A reconstruction strategy for echo planar spectroscopy and its application to partially undersampled imaging

[1,2]LARS G. HANSON, [2]KJELD SCHAUMBURG, [1]OLAF B. PAULSON

[1]Danish Research Center for Magnetic Resonance

Hvidovre Hospital

Copenhagen, Denmark

[2] CISMI, Department of Chemistry

University of Copenhagen, Denmark

Running head: A reconstruction strategy for echo planar spectroscopy

Accepted: *Magnetic Resonance in Medicine*

Version: April 19, 2000

Correspondence to:

Lars G. Hanson

Danish Research Center for Magnetic Resonance

Hvidovre Hospital, afs. 340

Kettegård Allé 30

DK-2650 Hvidovre

Denmark

Phone: +45 36 32 29 76

Fax: +45 36 47 03 02

email: larsh@magnet.drcmr.dk

Abstract

The most commonly encountered form of echo planar spectroscopy (EPS) involves oscillating gradients in one spatial dimension during readout. Data are consequently not sampled on a Cartesian grid. A fast gridding algorithm applicable to this particular situation is presented. The method is optimal, i.e., it performs as well as the full discrete Fourier transform (DFT) for band limited signals while allowing for use of the fast Fourier transform (FFT). The method is demonstrated for reconstruction of data that are partially undersampled in the time domain. The advantages of undersampling are lower hardware requirements or fewer interleaves per acquisition. The method is of particular interest when large bandwidths are needed (eg., for high field scanning) and for scanners with limited gradient performance. The unavoidable artifacts resulting from undersampling are demonstrated to be acceptable for spectroscopy with long echo times.

Key words: echo planar spectroscopy; reconstruction; undersampling;
magnetic resonance spectroscopy

1 INTRODUCTION

Echo planar spectroscopy (EPS) proposed by Mansfield (1) offers rapidly acquired data for spatially resolved spectroscopic studies, (2–4). Several variants have been implemented (5–11). The common feature is that data are acquired in the presence of an oscillating readout gradient, while differences occur in methods for water and lipid suppression, spatial selection, excitation and gradient schemes.

This paper addresses aspects of sequence design and reconstruction for a simple EPS scheme involving an oscillating gradient in just one direction and phase encoding in the remaining spatial dimensions.

Data are sampled non-equidistantly in (k, t)-space as shown in Fig. 1, and artifacts must be traded off for reconstruction time and computational complexity. The simplest approach is to ignore spin evolution not caused by imaging gradients in the readout periods. This allows for fast reconstruction using the FFT algorithm, and it works particularly well with spectral oversampling (8, 12). Alternatively, reconstruction can be done using DFT directly. The optimal performance of the DFT is obtained at the expense of reconstruction time ($O(N^4)$ for 2D-DFT of N^2 points versus $O(N^2 \log_2 N)$ for 2D-FFT). Another approach is gridding, representing a flexible compromise.

We present a gridding algorithm tailored for the problem at hand. It takes advantage of the localization of the sample points on straight lines in (k, t)-space (13, 14). The merits of the method are speed and optimal performance i.e., performance as good as that of the full DFT.

The method is demonstrated for undersampled spectroscopy, i.e., when the gradient oscillation period $2T$ (Fig. 1) exceeds the sample interval required for resolving all metabolite signals. Undersampling minimizes hardware and interleaving requirements and provides a fast alternative to oversampling (1).

The article is organized as follows: The spectroscopic sequence relying on undersampling is described. General properties of the reconstruction are discussed as well as its application to adequately sampled and undersampled data. Finally, examples of *in vitro*

and *in vivo* spectra are presented.

2 METHODS

2.1 THE SPECTROSCOPIC SEQUENCE

A multi-slice EPS sequence was implemented on a Siemens Vision 1.5 T whole-body scanner. The sequence is conceptually similar to implementations by other groups (5–8). The main difference is a low acquisition bandwidth and non-interleaved sampling. Each cycle consists of outer volume and water suppression, slice-selective excitation and refocusing, phase encoding followed by data-acquisition in presence of an oscillating readout gradient. This is repeated for each slice and each line of k-space. The oscillating readout gradient is initiated one cycle ahead of actual sampling to reduce effects of transient eddy currents. Each half-cycle consists of 0.2 ms sinusoidal gradient inversion and a 3.2 ms readout period with constant gradient. One dimension in k-space is consequently traversed 64 times during a 217.6 ms readout period giving a spectral range of 294 Hz (4.6 ppm at 1.5 Tesla).

2.2 POST-PROCESSING

Reconstruction A spatial shift appears when the data from a particular gradient echo are reconstructed without accounting for spin evolution not caused by imaging gradients in the readout periods. The sign of the shift depends on the polarity of the readout gradient that differs between even and odd echoes. The bandwidth per pixel was 312 Hz for the implemented sequence corresponding to a shift of half a pixel of the N-acetylaspartate(NAA) signal relative to water. A reconstruction to be discussed in detail, was developed to avoid the corresponding spatial broadening.

The discussion is limited to the relevant spatial (readout) and frequency dimensions (x, ν) and the corresponding reciprocal space (k, t) in which data are collected. These quantities are all taken to be dimensionless so that x and ν are given in units of the spatial and spectral resolution respectively. The correction for spatial shifts of metabolites amounts

to an interpolation of data in (k,t)-space to a grid. Such an interpolation can be done perfectly if the Nyquist criterion is fulfilled. Artifact free reconstruction can therefore be performed to a bandwidth equal to the minimum sampling rate of the signal, i.e., $1/(2T)$ in Fig. 1, if the signal is equally band limited. Reconstruction is conveniently performed on even and odd echoes separately, since samples are equidistantly collected along straight lines in (k,t)-space as shown in Fig. 1. A correction for these lines not being parallel to the $t = 0$ line can be done using the Fourier shift theorem. The shift corresponding to the frequency ν is ν/b, where b is the acquisition bandwidth per pixel given by the inverse of the readout time RO, $b = 1/\text{RO}$. Corrected signal matrices $\tilde{S}_{even}$ and $\tilde{S}_{odd}$ can be constructed from the even and odd echo signal matrices, $S_{even}(k,\nu)$ and $S_{odd}(k,\nu)$ according to

$$\tilde{S}_{even}(k,\nu) = \exp(-ik\nu/b)S_{even}(k,\nu) \quad [1]$$

$$\tilde{S}_{odd}(k,\nu) = \exp(ik\nu/b)S_{odd}(k,\nu) \quad [2]$$

Two applications of these equations are of interest: Water reference reconstruction and reconstruction of oversampled metabolite data. After shimming, protons in water precess at a frequency range of a few Hertz around the carrier frequency being adjusted to the water resonance. Half bandwidth reconstruction is therefore sufficient. Signals from unsuppressed lipids can be filtered out, and spatial reconstruction completing the half-bandwidth reconstruction is rapidly performed using FFT.

The other and more interesting use of Eq. [1-2] is for metabolite reconstruction, when spectral oversampling is employed, i.e., when half bandwidth reconstruction is enough for resolving all metabolite signals. The appropriate frequency range in this case is $[-1/(2T); 0]$ since the metabolites are known to oscillate at negative frequencies relative to water. Any residual water signal must be removed before applying the correction to avoid large spatial shifts of positive low-frequency components.

The hardware demands can be reduced without increasing the number of k-space interleaves if sampling is performed with the readout gradient oscillating at only half the Nyquist frequency. In this case, half bandwidth reconstruction provided by Eq. [1-2] is insufficient. In order to do full spatial and spectral bandwidth reconstruction of the metabolite

data, the two corrected datasets must be appropriately combined.

A corrected signal matrix $\tilde{S}$ can be constructed using Danielson-Lanczos lemma (15). This is illustrated in Fig. 2 and is expressed by the equation

$$\tilde{S}(k,\nu) = \exp(-ik\nu/b)S_{even}(k,\nu) + \exp(i2\pi\nu T)\exp(ik\nu/b)S_{odd}(k,\nu) \qquad [3]$$

The signals S_{even} and S_{odd} are periodic in frequency ν with period $1/(2T)$. The exponential factor $\exp(i2\pi\nu T)$ (period $1/T$) accounts for the time shifts of the odd echoes with respect to even echoes. Consequently $\tilde{S}(k,\nu)$ provides spectral information over the full frequency range, $1/T$. This corresponds to optimal gridding in the (k,t) domain, and the remaining steps of the reconstruction is common to those outlined for half bandwidth reconstruction. The reconstruction Eq. [3] is exact if the Nyquist criterion is fulfilled for all frequencies.

Water referencing and subtraction Water referencing was performed pixel-wise in the reconstructed data sets. The water suppressed metabolite signal in each voxel was divided by the complex phase of the water signal (16, 17).

Any residual water signal must be removed before Eq. [3] is applied: Signals oscillating at slightly higher frequencies than the carrier are spatially far displaced, since the correction is designed to correct metabolite signals that are known to oscillate at negative frequencies. Any residual water peak will suffer severe line shape distortion and spatial broadening. The residual water signal was removed by subtracting the projection onto a space spanned by five vectors constructed as the water reference signal frequency shifted by a fraction of the water linewidth. The projection was performed using singular value decomposition (15).

2.3 EXPERIMENTAL VERIFICATION

Phantom and *in vivo* experiments were performed for validation of the reconstruction procedure and for comparison with standard FFT that is a conventional approach. Four slice acquisition with echo and repetition times of 144 ms and 1.5 second was used for all experiments.

For calculating phantom metabolite maps, two water suppressed measurements and a reference scan were acquired in three minutes (each of one minute duration). The phantom contained 10 mM solutions of substances spectroscopically similar to the metabolites detectable at long echo times. These were present in tubes embedded in a larger cylinder with an acetone solution (similar to 10 mM NAA).

The *in vivo* data were acquired in 10 minutes from four axial slices through the brain of a healthy volunteer. Six one minute acquisitions (1 ml isotropic voxels) were obtained along with six additional 30 second acquisitions of the central 50 percent of k-space (full range in the readout-direction, half range in the phase encoding direction). This weighted k-space acquisition scheme improves the spatial impulse response with little sacrifice of efficiency (18, 19). The water reference data set was obtained in one minute.

3 RESULTS

The spatial and spectral resolutions are closely linked and two-dimensional point spread functions (PSFs, (1)) were calculated. Results of theoretical evaluations of the broadening are illustrated in Fig. 3: A point source is located in the middle of a 16 voxel FOV interpolated to 32 voxels by zero-filling. The source is chosen to oscillate at the NAA frequency with a signal decay time $T_2^* = 65$ ms. This frequency is 37 in units of the bandwidth per point for $T = 3.4$ ms. A main peak is seen at the metabolite frequency in Fig. 3(a,b) as well as spectral ghosts displaced by half the spectral range that is 32 in these units. Profiles through the PSFs are given in Fig. 3(c,d,e) as well as comparisons to the non-broadened case (the normal sinc function).

Figure 4 demonstrates the spatial broadening and how it is suppressed by proper reconstruction. Large differences between images reconstructed from the first even and odd echoes appear close to edges perpendicular to the readout gradient when the carrier frequency is adjusted 200 Hz off-resonance. This was done to make water oscillate relative to the carrier frequency as would lactate relative to a carrier adjusted to water.

Metabolite maps resulting from standard FFT and from the corrected reconstruction

algorithms of phantom data are shown in Fig. 5. The nature of spectral ghosts is illustrated in Fig. 6 that show spectral images evaluated at frequencies where ghosts are expected.

Finally, an *in vivo* example of a metabolite map and a spectrum from a 1 ml white matter voxel is shown in Fig. 7.

4 DISCUSSION

The reconstruction presented offers enhanced spatial resolution compared to standard FFT applied to the non-uniformly sampled data as shown in Fig. 3. This was demonstrated in theory in Fig. 3 as well as in practice (Figs. 4 and 5). The residual edge artefacts in Fig. 4 can be attributed to the substances other than water in this spectroscopy phantom.

Improved spatial homogeneity is found in Fig. 5. This could be a result of unforeseen spatial broadening rather than a result of accounting for the (k, t)-space trajectory. The observed intensity increase for the narrow tubes is, however, consistent with the expected spatial narrowing, thus showing that the algorithm provides improved overall image quality including better spatial resolution as expected. Residual spatial broadening over a length of $\delta x = \delta\nu/b$ proportional to the spectral width $\delta\nu$ of the metabolite signal can be expected considering the nature of the reconstruction illustrated in Fig. 2.

The PSFs differ from metabolite to metabolite for uncorrected data due to the chemical shift dependent displacement. The advantage of the improved reconstruction is greater for Lac and NAA compared to Cho and Cr, as can be seen in Fig. 5.

Undersampled imaging is a natural candidate for the method, as artifacts from the non-Cartesian sampling are worst for low-bandwidth acquisition. The resulting spectral ghosts appear at positions, where there are spatial variations in the metabolite concentrations. The ghosts demonstrated theoretically in Fig. 3 are particularly visible in the spectral image evaluated at the Cr frequency plus half a spectral bandwidth as shown in Fig. 6 (the SNR is too low to make the feeble ghosts fully visible for the other substances). The magnitudes of the ghosts are largely unaffected by the reconstruction procedure, as can be anticipated from Fig. 2.

Ghosts are not necessarily a problem as demonstrated in Figs. 5 and 6: They are shifted by half the spectral range, which is 4.6 ppm in the present study. This was chosen to avoid overlap of any of the primary metabolites detectable at long echo times (NAA (2.0 ppm), Cr (3.0 ppm), Cho (3.2 ppm), Lac (1.3 ppm)) and their respective ghosts. A water ghost would appear in the middle of the spectrum (2.4 ppm), which is one reason that water signals must be carefully suppressed or removed in post-processing prior to the correction. The residual artifacts were not found to be problematic for evaluation of peak intensities.

Finally, inadequately suppressed lipid signals will result in ghosts that overlap with the Cho and Cr signals. Undersampling is problematic if other metabolites are of interest e.g., for spectroscopy with short echo times.

The representative brain spectrum in Fig. 7 illustrates the performance of the undersampling sequence *in vivo*. High spatial resolution spectra from multiple slices can be obtained rapidly (1 ml resolution, one minute per acquisition/10 minutes total scanning).

Finally it must be noticed that standard FFT does not provide an alternative to spatial filtering even though the side bands are somewhat suppressed compared to the suggested algorithm as seen in Fig. 3(a,b). Parsevals theorem (15) implies that the noise amplitudes are equal for the standard FFT and the proposed reconstruction and the normal SNR gain caused by filtering is therefore not provided by standard FFT even though the resulting PSFs are somewhat similar. If spatial filtering is wanted, it is best applied to the corrected data $\tilde{S}(k, \nu)$.

5 Conclusion

Inherent spin evolution during signal readout cause spatial broadening if not accounted for with gridding or DFT reconstruction. A fast and optimal gridding algorithm relying on FFT was demonstrated. Like other reconstruction methods, it does not remove ghosts resulting from spectral undersampling, but ghosts were shown not to cause problems for long echo time spectroscopy. The advantages of undersampling are short gradient switching time and low hardware requirements with respect to gradient and eddy current performance. This

performance was obtained without interleaved acquisition that prolongs acquisition times.

The main potential of the undersampling strategy is for echo planar spectroscopy using clinical scanners, where the hardware performance is often limited, and using high field scanners, where fast gradient oscillation is needed for resolving all metabolite signals.

6 ACKNOWLEDGMENTS

The authors wish to thank Elfar Adalsteinsson and Dan Spielman for useful comments regarding the manuscript. This work was supported by the EU under contract number PL 95 0861 and by the University of Copenhagen.

REFERENCES

1. P. MANSFIELD, Spatial mapping of the chemical shift in NMR. *Magn Reson Med* **1**, 370-86 (1984).

2. S. POSSE, S. R. DAGER, T. L. RICHARDS, C. YUAN, R. OGG, A. A. ARTRU, H. W. MULLER-GARTNER, AND C. HAYES, *In vivo* measurement of regional brain metabolic response to hyperventilation using magnetic resonance: Proton echo planar spectroscopic imaging (PEPSI). *Magn Reson Med* **37**, 858-65 (1997).

3. A. C. HEIDE, G. H. KRAFT, J. C. SLIMP, J. C. GARDNER, S. POSSE, S. SERAFINI, J. D. BOWEN, AND T. L. RICHARDS, Cerebral N-acetylaspartate is low in patients with multiple sclerosis and abnormal visual evoked potentials. *Am J Neuroradiol* **19**, 1047-54 (1998).

4. K. O. LIM, E. ADALSTEINSSON, D. SPIELMAN, E. V. SULLIVAN, M. J. ROSENBLOOM, AND A. PFEFFERBAUM, Proton magnetic resonance spectroscopic imaging of cortical gray and white matter in schizophrenia. *Arch Gen Psychiatry* **55**, 346-52 (1998).

5. S. MATSUI, K. SEKIHARA, AND H. KOHNO, Spatially resolved NMR spectroscopy using phase-modulated spin-echo-trains. *J Magn Reson* **67**, 476-490 (1986).

6. D. N. GUILFOYLE, A. BLAMIRE, B. CHAPMAN, R. J. ORDIDGE, AND P. MANSFIELD, PEEP–a rapid chemical-shift imaging method. *Magn Reson Med* **10**, 282-7 (1989).

7. P. WEBB, D. SPIELMAN, AND A. MACOVSKI, A fast spectroscopic imaging method using a blipped phase encode gradient. *Magn Reson Med* **12**, 306-15 (1989).

8. S. POSSE, C. DECARLI, AND D. LE BIHAN, Three-dimensional echo-planar MR spectroscopic imaging at short echo times in the human brain. *Radiology* **192**, 733-8 (1994).

9. E. ADALSTEINSSON, P. IRARRAZABAL, D. M. SPIELMAN, AND A. MACOVSKI, Three-dimensional spectroscopic imaging with time-varying gradients. *Magn Reson Med* **33**, 461-6 (1995).

10. S. HIRATA, Y. BITO, AND E. YAMAMOTO, Expansion of the spectral bandwidth by spatial and chemical shift selective saturation in high-speed magnetic resonance spectroscopic imaging. *Magn Reson Med* **35**, 611-6 (1996).

11. E. ADALSTEINSSON, P. IRARRAZABAL, S. TOPP, C. MEYER, A. MACOVSKI, AND D. M. SPIELMAN, Volumetric spectroscopic imaging with spiral-based k-space trajectories. *Magn Reson Med* **39**, 889-98 (1998).

12. S. POSSE, G. TEDESCHI, R. RISINGER, R. OGG, AND D. LE BIHAN, High speed ^{1}H spectroscopic imaging in human brain by echo planar spatial-spectral encoding. *Magn Reson Med* **33**, 34-40 (1995).

13. T. R. BROWN, B. M. KINCAID, AND K. UGURBIL, NMR chemical shift imaging in three dimensions. *Proc Natl Acad Sci USA* **79**, 3523-6 (1982).

14. D. B. TWIEG, The k-trajectory formulation of the NMR imaging process with applications in analysis and synthesis of imaging methods. *Med Phys* **10**, 610-21 (1983).

15. W. PRESS, S. TEUKOLSKY, W. VETTERLING, AND B. FLANNERY, "Numerical Recipes in C (The Art of Scientific Computing)". Cambridge University Press, 1992.

16. D. SPIELMAN, P. WEBB, AND A. MACOVSKI, Water referencing for spectroscopic imaging. *Magn Reson Med* **12**, 38-49 (1989).

17. U. KLOSE, *In vivo* proton spectroscopy in presence of eddy currents. *Magn Reson Med* **14**, 26-30 (1990).

18. T. H. MARECI AND H. R. BROOKER, High-Resolution Magnetic Resonance Spectra from a Sensitive Region Defined with Pulsed Field Gradients. *J Magn Reson* **57**, 157-163 (1984).

19. D. L. PARKER, G. T. GULLBERG, AND P. R. FREDERICK, Gibbs artifact removal in magnetic resonance imaging. *Med Phys* **14**, 640-5 (1987).

Figure captions

Figure 1: Sampling strategy in (k, t)-space, where k is the spatial frequency and t is time. The trajectory is shown for two periods of readout gradient oscillation. The time evolution of the maximum frequency, k_{max}, is effectively only probed once every gradient oscillation period $2T$, while the zero frequency is sampled twice as often.

Figure 2:

Schematic overview of the reconstruction algorithm illustrating the spectral-spatial signal densities resulting from an oscillating point source. (a) A signal with a single frequency component ν_0 originating from position x_0 ($\otimes$) gives rise to two spatially displaced peaks ($\bigcirc$) in the frequency range $[0; -1/T]$ after reconstruction of odd echo images due to the periodicity of the Fourier transform, (b). The peaks are displaced in the opposite direction for the even echo ($\times$). (c) The proposed algorithm shifts both sets of peaks according to their frequency. The true peaks overlap at the original position, while the aliased ones are shifted too much to cancel. (d) The shifts are too small to cause ghost cancellation for a point source oscillating at a frequency in the interval $[-1/(2T); -1/T]$.

Figure 3: Spectral-spatial PSFs for NAA using (a) standard and (b) corrected FFT reconstruction. Details regarding the calculation and the units are given in the results section. The main lobe is seen at the metabolite frequency (37 in units of the bandwidth per pixel) as well as spectral ghosts displaced by half the spectral range that is 32 in these units. (b) Substantial spatial narrowing results from the correction. This graph is conceptually similar to Fig. 2(c). The image intensities are illustrated in (c,d,e) showing uncorrected (dotted) and corrected profiles (solid) through the PSFs using a common vertical scale. Dashed curves (almost completely overlapping with the corrected profiles in (c,d)) illustrate the PSF in the absence of artifacts, i.e., in the limit of rapid gradient oscillation. The correction restores the spatial (c) and spectral (d) profiles through the main lobe of the PSF almost entirely, while the spatial profile through the ghosts is nearly unaffected by the correction, (e).

Figure 4: Effects of correction for odd/even echo asymmetry. (a) Localizer image of water-filled tube phantom with saturation slices covering test tubes containing vegetable oil. (b) Corresponding zero-filled water reference image with the carrier adjusted to water. The carrier was subsequently adjusted 200 Hz up to make water oscillate as would lactate. (c) and (d) show the resulting absolute difference images between images reconstructed from the first even and odd echoes acquired with opposite gradient polarity. (c) Shift artifacts are clearly visible near vertical edges for standard FFT reconstruction. (d) Using Eq. [3], the maximum intensity of the edge artifacts is reduced by a factor of four compared to (c), and the image intensity is scaled up accordingly.

Figure 5: *In vitro* comparison of reconstruction algorithms. Normalized absolute spectral images $|S(x, y, \nu)|$ are shown corresponding to NAA, Cho, Cr and Lac frequencies (the low frequency component of the Lac doublet). The proposed reconstruction algorithm is found to provide sharper contours and better homogeneity than standard FFT reconstruction. The peak intensity in the small tubes are larger in (a) compared to (b) by 7%, 4% and 24% for Cho, Cr, and Lac respectively (averaged over the widths of the tubes in the phase encoding direction). This is consistent with the expected spatial frequency-dependent narrowing in the readout direction.

Figure 6: Absolute spectral ghost images corresponding to the metabolite images in Fig. 5(a) calculated as $S(x, y, (\nu + (2T)^{-1})$ modulo $T^{-1})$, i.e., images at frequencies displaced by half the spectral bandwidth. Low intensity spectral ghost are visible near vertical edges. These result from undersampling and are common for the two reconstruction techniques.

Figure 7: (a) Example spectrum from an isotropic 1 ml voxel located mainly in white matter as indicated with a box on the inset water reference image (left). The right inset is the measured NAA map in the same slice. This four slice study was performed in 10 minutes.

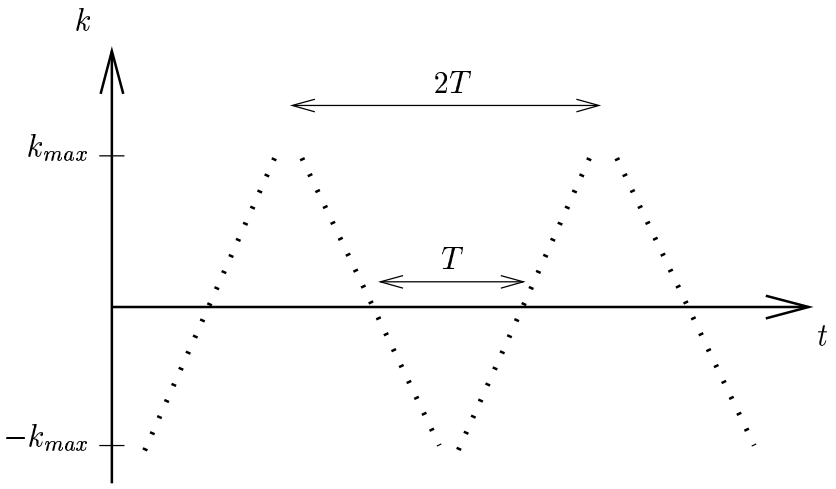

Figure 1:

Sampling strategy in (k, t)-space, where k is the spatial frequency and t is time. The trajectory is shown for two periods of readout gradient oscillation. The time evolution of the maximum frequency, k_{max}, is effectively only probed once every gradient oscillation period $2T$, while the zero frequency is sampled twice as often.

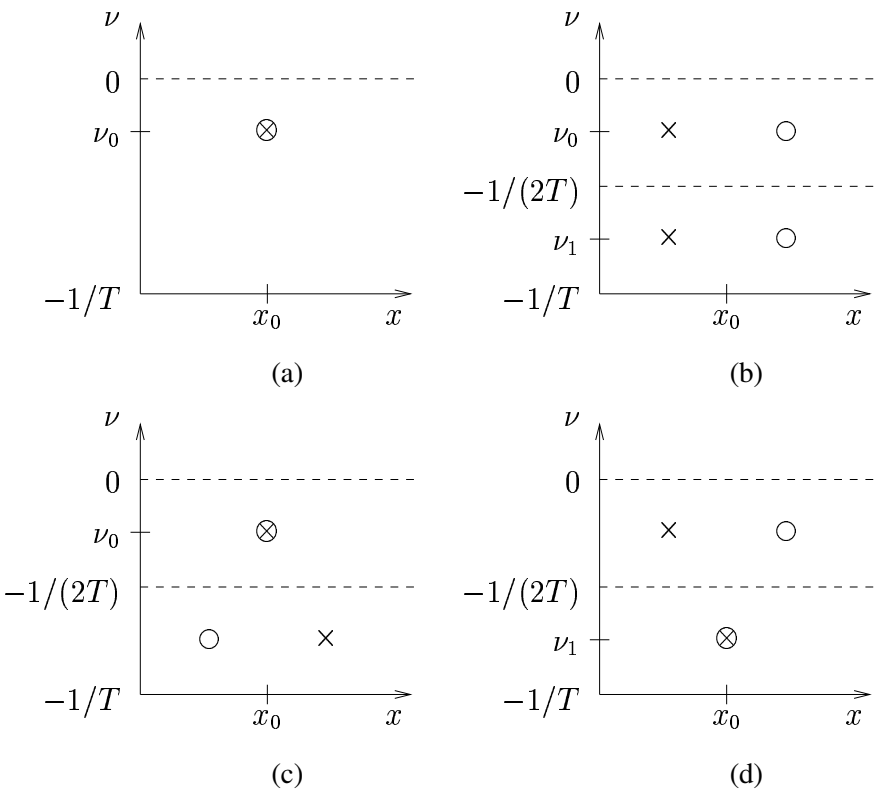

Figure 2:

Schematic overview of the reconstruction algorithm illustrating the spectral-spatial signal densities resulting from an oscillating point source. (a) A signal with a single frequency component ν_0 originating from position x_0 ($\otimes$) gives rise to two spatially displaced peaks ($\bigcirc$) in the frequency range $[0; -1/T]$ after reconstruction of odd echo images due to the periodicity of the Fourier transform, (b). The peaks are displaced in the opposite direction for the even echo ($\times$). (c) The proposed algorithm shifts both sets of peaks according to their frequency. The true peaks overlap at the original position, while the aliased ones are shifted too much to cancel. (d) The shifts are too small to cause ghost cancellation for a point source oscillating at a frequency in the interval $[-1/(2T); -1/T]$.

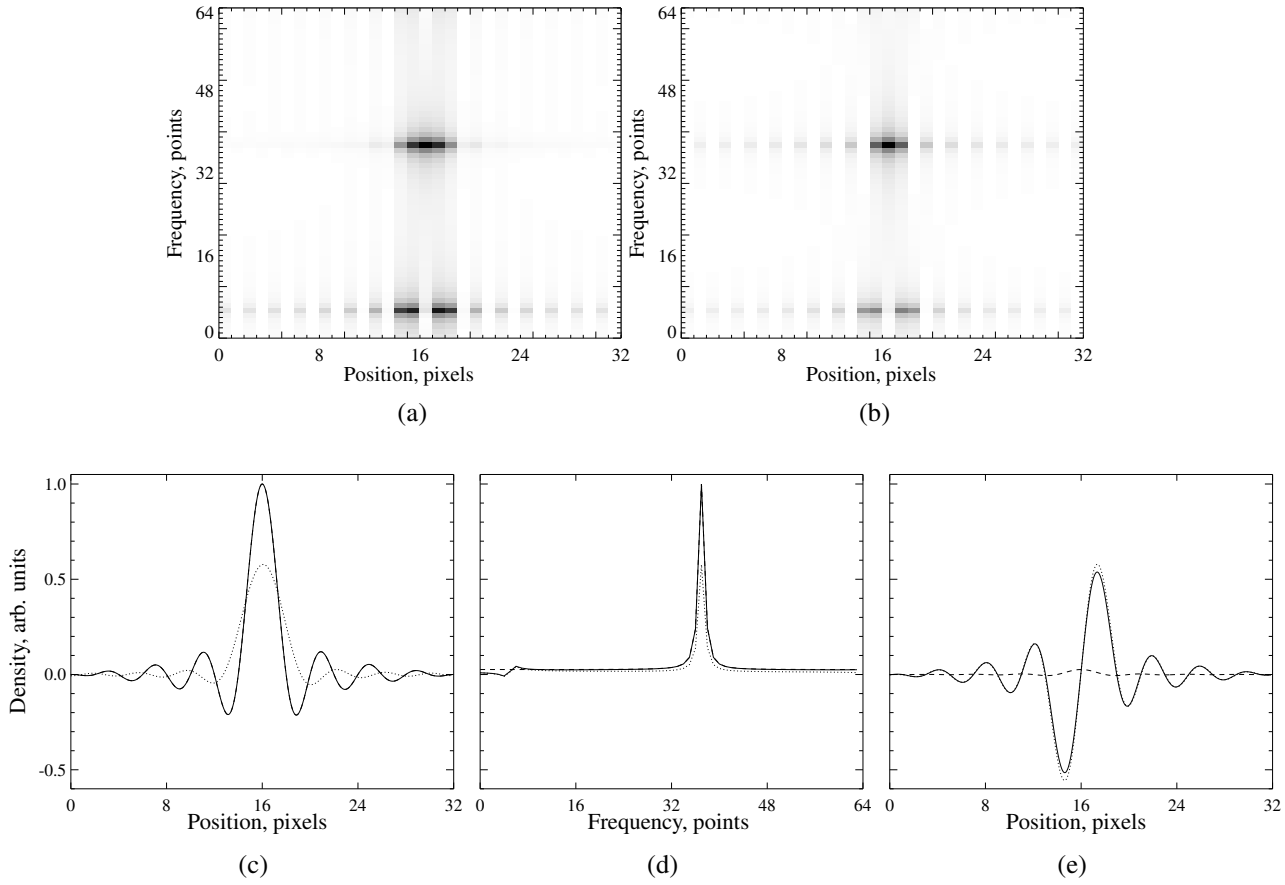

Figure 3:

Spectral-spatial PSFs for NAA using (a) standard and (b) corrected FFT reconstruction. Details regarding the calculation and the units are given in the results section. The main lobe is seen at the metabolite frequency (37 in units of the bandwidth per pixel) as well as spectral ghosts displaced by half the spectral range that is 32 in these units. (b) Substantial spatial narrowing results from the correction. This graph is conceptually similar to Fig. 2(c). The image intensities are illustrated in (c,d,e) showing uncorrected (dotted) and corrected profiles (solid) through the PSFs using a common vertical scale. Dashed curves (almost completely overlapping with the corrected profiles in (c,d)) illustrate the PSF in the absence of artifacts, i.e., in the limit of rapid gradient oscillation. The correction restores the spatial (c) and spectral (d) profiles through the main lobe of the PSF almost entirely, while the spatial profile through the ghosts is nearly unaffected by the correction, (e).

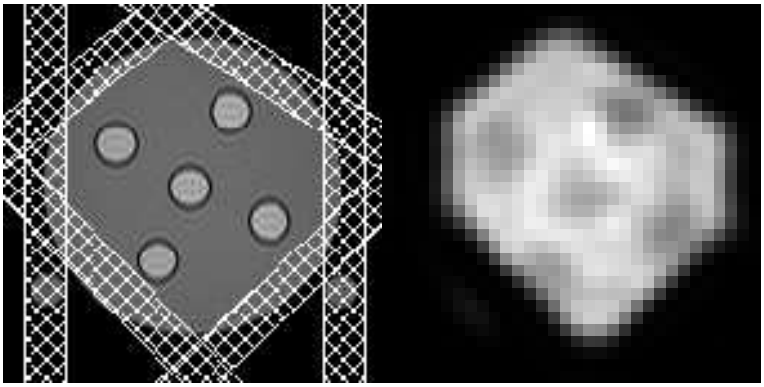

(a) (b)

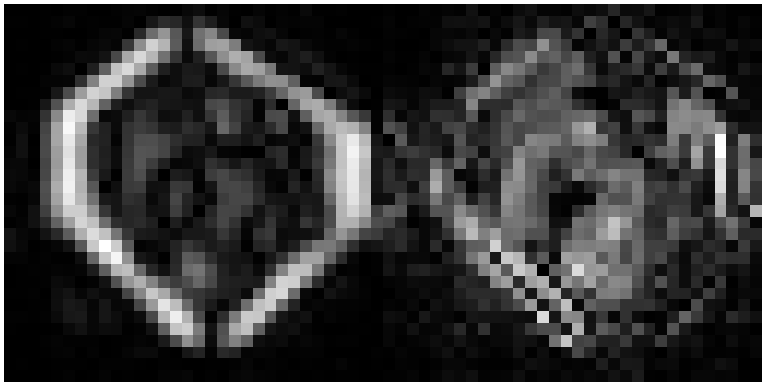

(c) (d)

Figure 4:

Effects of correction for odd/even echo asymmetry. (a) Localizer image of water-filled tube phantom with saturation slices covering test tubes containing vegetable oil. (b) Corresponding zero-filled water reference image with the carrier adjusted to water. The carrier was subsequently adjusted 200 Hz up to make water oscillate as would lactate. (c) and (d) show the resulting absolute difference images between images reconstructed from the first even and odd echoes acquired with opposite gradient polarity. (c) Shift artifacts are clearly visible near vertical edges for standard FFT reconstruction. (d) Using Eq. [3], the maximum intensity of the edge artifacts is reduced by a factor of four compared to (c), and the image intensity is scaled up accordingly.

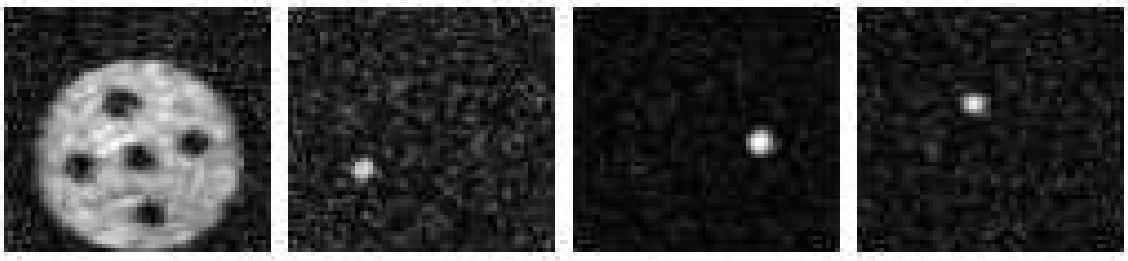

(a) Reconstruction using the proposed algorithm.

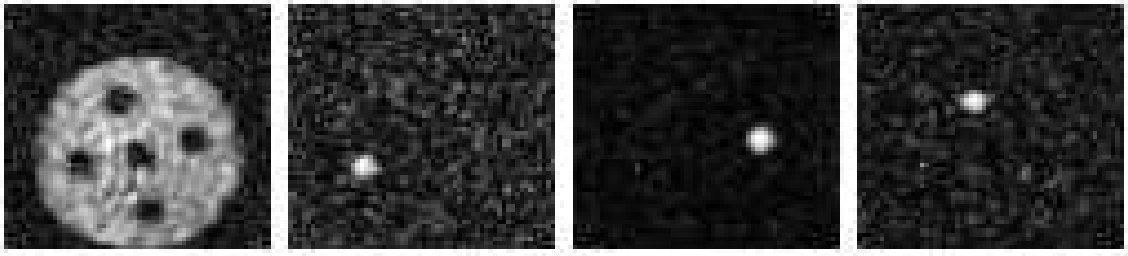

(b) Reconstruction using standard FFT.

Figure 5:

In vitro comparison of reconstruction algorithms. Normalized absolute spectral images $|S(x, y, \nu)|$ are shown corresponding to NAA, Cho, Cr and Lac frequencies (the low frequency component of the Lac doublet). The proposed reconstruction algorithm is found to provide sharper contours and better homogeneity than standard FFT reconstruction. The peak intensity in the small tubes are larger in (a) compared to (b) by 7%, 4% and 24% for Cho, Cr, and Lac respectively (averaged over the widths of the tubes in the phase encoding direction). This is consistent with the expected spatial frequency-dependent narrowing in the readout direction.

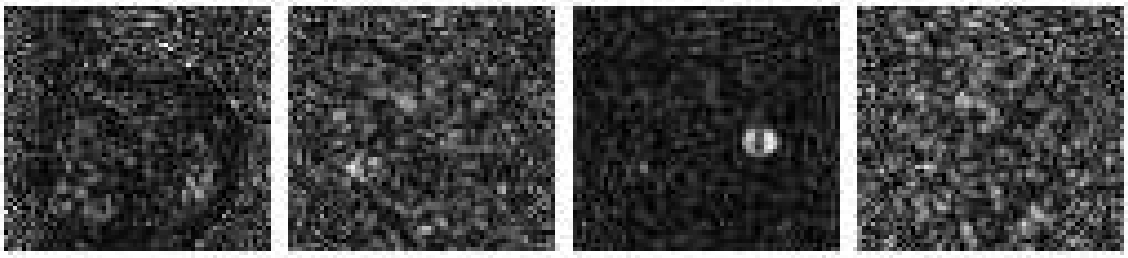

Figure 6:

Absolute spectral ghost images corresponding to the metabolite images in Fig. 5(a) calculated as $S(x, y, (\nu + (2T)^{-1})$ modulo $T^{-1})$, i.e., images at frequencies displaced by half the spectral bandwidth. Low intensity spectral ghost are visible near vertical edges. These result from undersampling and are common for the two reconstruction techniques.

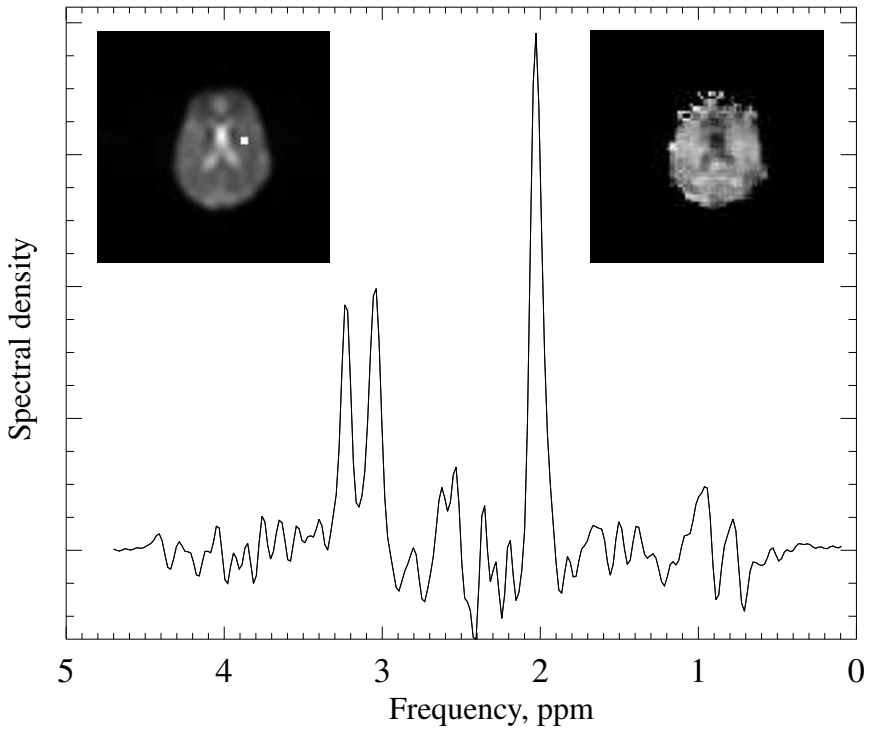

Figure 7:

(a) Example spectrum from an isotropic 1 ml voxel located mainly in white matter as indicated with a box on the inset water reference image (left). The right inset is the measured NAA map in the same slice. This four slice study was performed in 10 minutes.